

# Coseismic and Postseismic Fault Slip for the 17 August 1999, $M = 7.5$ , Izmit, Turkey Earthquake

R. E. Reilinger,<sup>1\*†</sup> S. Ergintav,<sup>2†</sup> R. Bürgmann,<sup>3†</sup> S. McClusky,<sup>1</sup>  
O. Lenk,<sup>4</sup> A. Barka,<sup>5</sup> O. Gurkan,<sup>6</sup> L. Hearn,<sup>1</sup> K. L. Feigl,<sup>7</sup>  
R. Cakmak,<sup>2</sup> B. Aktug,<sup>4</sup> H. Ozener,<sup>6</sup> M. N. Töksoz<sup>1</sup>

We use Global Positioning System (GPS) observations and elastic half-space models to estimate the distribution of coseismic and postseismic slip along the Izmit earthquake rupture. Our results indicate that large coseismic slip (reaching 5.7 meters) is confined to the upper 10 kilometers of the crust, correlates with structurally distinct fault segments, and is relatively low near the hypocenter. Continued surface deformation during the first 75 days after the earthquake indicates an aseismic fault slip of as much as 0.43 meters on and below the coseismic rupture. These observations are consistent with a transition from unstable (episodic large earthquakes) to stable (fault creep) sliding at the base of the seismogenic zone.

By measuring the displacement of Earth's surface during and after an earthquake (coseismic and postseismic, respectively), it is possible to estimate the distribution of fault slip along the rupture (1–3). Mapping the spatial distribution of fault slip provides clues about the mechanics of the earthquake process and the mechanical behavior of the upper layers of Earth (4–6). Understanding the distribution of coseismic and postseismic fault slip also has implications for evaluating the potential for neighboring faults to generate future earthquakes (7–10).

The mid- to lower-crustal structure and rheology of major strike-slip faults may be represented as a zone of broadly distributed ductile flow (11–14), a narrow shear zone that extends through much of the crust and possibly the upper mantle (4, 5, 15, 16), or a combination of localized faulting and distributed ductile shear during different times in the earthquake cycle (6, 17). Two-dimensional model calculations show that predicted

surface deformation due to aseismic slip or viscoelastic flow below the brittle upper crust are difficult to distinguish, both for steady interseismic deformation and postseismic deformation transients along major strike-slip faults (18, 19). However, both the temporal pattern and spatial distribution of deformation transients in response to large earthquakes continue to shed light on earthquake mechanics and fault zone rheology at depth (20).

**GPS evidence for coseismic and postseismic displacements.** Here, we used GPS observations made before and after the Izmit earthquake to estimate the displacements that accompanied (Fig. 1) and followed (first 75 days) (Fig. 2) the earthquake (21). Because the Marmara Sea region had been identified as a seismic gap capable of generating large earthquakes (8, 22, 23), a network of continuous GPS stations and survey-mode GPS sites had been established before the earthquake (24–27). Five of the continuous GPS stations operating before the Izmit earthquake were within the coseismic deformation field (Fig. 1). Four more continuously recording stations were installed within 48 hours of the main shock to track postseismic deformation (Fig. 2). Eight days following the main shock, we began to remeasure the positions of many of the survey sites displaced by the earthquake. Of the 51 survey sites at which we determined coseismic displacements for the 17 August 1999 shock, 33 were occupied at least twice and 18 at least three times in the first 2 months after the event. Our postseismic analysis includes data from 35 sites that span sufficiently long time periods during this time interval (Fig. 2).

The GPS data were processed with standard procedures using the GAMIT GPS processing software (27). To estimate coseismic displacements, we used a simple, linear-in-time model for elastic strain accumulation to extrapolate the station position measured before the earthquake to the time immediately preceding the shock (28). Similarly, we used the elastic model for the postseismic after-slip reported here to extrapolate positions measured after the earthquake back to the time immediately after the main shock (29). Although the continuously operating stations show that deformation rates varied somewhat during the 75-day, postseismic observation period (21), we estimated linear postseismic displacement rates from a weighted least squares procedure using the station coordinates and their covariances. The observed postseismic displacements are corrected for background secular motions using predicted interseismic model velocities at each site (28). This procedure allows us to produce a consistent set of 75-day displacements from data spanning different postseismic time periods.

**Coseismic fault model.** We used the mapped coseismic surface rupture to determine the location of the fault used in our model (30–32). Beneath Izmit Bay (the narrow E-W oriented bay extending east from the Marmara Sea in Fig. 1) we used the distribution of aftershocks (33) and fault maps based on submarine and coastal morphology (34) to locate the coseismic fault model. The trace of the resulting modeled fault follows the southern shoreline of Izmit Bay to the east side of the Hersek Delta (on southern shore of Izmit Bay, about 10 km SE of station TUBI in Fig. 1). There, it steps north and continues westward, coinciding with the aftershocks. This geometry reflects the lack of primary surface rupture at the Delta and tests how the fault slip terminates in the west. Our fault model includes five segments (Fig. 1) that are further discretized into 3 km by 3 km patches for the distributed slip inversions (Fig. 3B).

The right-lateral, strike-slip focal mechanism (35), the lack of a systematic dip-slip offset along the surface rupture (30–32), and the distribution of aftershock hypocenters indicate that the earthquake primarily involved right-lateral, strike-slip offsets on vertical fault segments. The GPS data also provide constraints on the location, strike, and dip of the fault, as well as the orientation of coseismic slip. A two-fault model determined from the GPS coseismic displacements (36) corresponds closely to the segmented fault model based on surface mapping and aftershock locations (Fig. 4).

We used the discretized five-segment fault model and rectangular dislocations in an elastic half-space (1) to represent strike-slip offsets at the time of the Izmit earthquake. We inverted the coseismic displacements for the

<sup>1</sup>Department of Earth, Atmospheric, and Planetary Sciences, Massachusetts Institute of Technology, E34, 42 Carleton Street, Cambridge, MA 02142, USA.

<sup>2</sup>TUBITAK, Marmara Research Center, Earth Science Research Institute, Gebze 41470, Turkey. <sup>3</sup>Department of Earth and Planetary Science, 301 McCone Hall, University of California, Berkeley, Berkeley, CA 94720, USA. <sup>4</sup>General Command of Mapping, Cebese, Ankara, Turkey. <sup>5</sup>Istanbul Technical University, Eurasia Earth Science Institute, Ayazaga, Istanbul, Turkey. <sup>6</sup>Kandilli Observatory, Bogazici University, Istanbul, Turkey. <sup>7</sup>Department of Terrestrial and Planetary Dynamics (UMR 5562) Centre National de Recherche Scientifique, 14 ave. E. Belin 31400 Toulouse, France.

\*To whom correspondence should be addressed. E-mail: reilinge@erl.mit.edu

†These authors contributed equally to the work.

optimal slip distribution and found models that minimized the misfit while preserving smoothness of the model slip distribution (37). Synthetic checkerboard tests suggest that we can resolve slip in shallow-crust patches on the scale of tens of km, except along the East Sapanca segment (21). Resolution is good along the Yalova segment, but some of the deeper slip patches are less well resolved in the inversion test in other areas. The mapped surface offsets show considerable scatter (Fig. 3A), but most are within the "envelope" of the modeled near-surface offsets (upper 3 km). The geodetic coseismic moment is  $M_0 = 1.7 \times 10^{20}$  Nm (Newton-meters), ( $M_w = 7.5$ , where  $M_w$  is the moment magnitude), consistent with the seismic moment reported for the main shock ( $M_0 = 1.9 - 2.0 \times 10^{20}$  Nm) (38, 39).

The weighted sum of the residuals of the distributed coseismic slip model (WRSS, weighted residual sum of squares) (Figs. 1 and 4) was reduced to 1577 (compared with WRSS = 6929 in the two-fault geometry inversion). The model accounts for the large majority of the estimated site displacements. However, residual displacements reach 10 cm for some stations, substantially larger than our estimated uncertainties for these sites. Many of these stations are located near the surface rupture (Fig. 4). We suspect that these residuals reflect inelastic deformation including localized ground failure, heterogeneous properties of the crust, and/or small-

scale complexities in fault geometry.

Coseismic fault slip falls off rapidly below 12 to 15 km and concentrates along three high-slip patches that roughly coincide with the three structurally distinct central fault segments (Golcuk, West Sapanca, and East Sapanca) (Fig. 3B). The highest slip occurs within the upper 10 km of the crust, and it reaches 5.7 m on the western Golcuk segment and 4.7 m on the West Sapanca segment east of the epicenter. These two slip patches are separated by a zone of lower slip (<2 m) that includes the earthquake hypocenter. Along the westernmost segment of the Izmit fault break, the slip falls off rapidly west of the Hersek Delta (i.e., on the Yalova fault segment), consistent with the absence of primary surface faulting on the Delta. There is a slip gap up to 10-km long between the eastern East Sapanca segment and the more northeast trending Karadere segment. Slip diminishes to insignificance on the easternmost 10 km of the modeled fault, where the Düzce segment experienced small amounts of surface slip during the 17 August 1999 event.

The western extent of the coseismic faulting is important for estimating seismic hazards along the Yalova fault segment as well as in the Marmara Sea/Istanbul area (10, 40). High rates of aftershock activity along this segment (Fig. 2) suggest that it either slipped in the event or experienced large increases in Coulomb stress loading. The GPS data do not allow slip in excess of about 0.6 m along the

Yalova segment past 10 to 15 km west of the Hersek Delta. The absence of primary surface faulting on the Delta and the preferred GPS fault slip solution (Fig. 3B) suggest little faulting along the Yalova segment, implying a continued risk of earthquake failure.

**Postseismic fault slip model.** The rapid deformation transients during the first two months after the Izmit earthquake are not consistent with deformation rates expected from viscous relaxation of a broadly deforming lower crust (41). We modeled the observed postseismic displacements by transient strike-slip faulting after the Izmit earthquake with the same procedure as we used to model coseismic displacements. The model fault geometry is identical to that for the coseismic model, but it extends to a depth of 40 km. We also included an additional segment along the trace of the 12 November Düzce rupture (Figs. 2 and 3C). The Izmit rupture plane and its downdip extension is discretized into 550 patches of 4 km by 4 km.

Maximum afterslip occurred below the coseismic rupture reaching a total of 43 cm during the first 75 days after the main shock (Fig. 3C). The cumulative geodetic moment during the 75-day period (17 August to 3 November) was  $M_0 = 2.91 \times 10^{19}$  Nm, the equivalent of a  $M_w = 7$  earthquake. This is about an order of magnitude more than the moment released in the aftershocks of the event (42), indicating that afterslip occurred aseismically. The model fits the observed

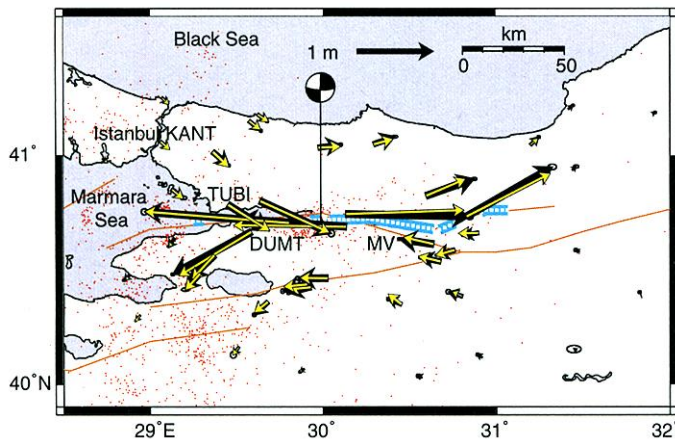
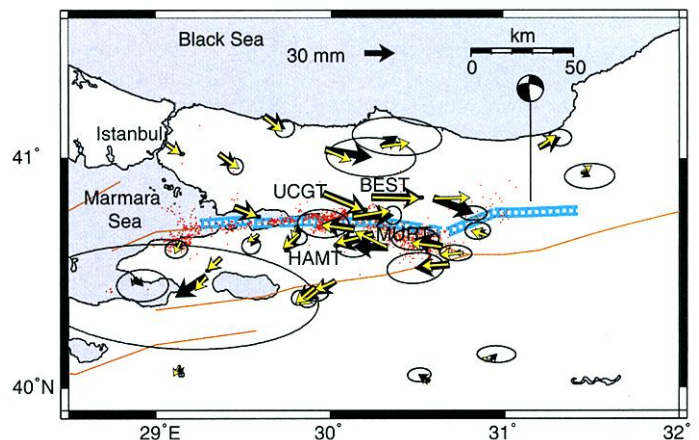


**Fig. 1. (left)** Map of Izmit region showing GPS sites and observed (including 95% confidence ellipses) and modeled (yellow arrows, using the slip distribution in Fig. 3B) horizontal coseismic displacements relative to a station in Ankara, Turkey (ANKR, located at 39.89°N, 32.76°E). Named sites (four-character ID) are continuous stations operating before and after the main shock; two additional continuous stations used in this study are located off the map at 40.61°N, 27.59°E, and 40.97°N, 27.96°E. Comparisons between observed and modeled vertical displacements and residual horizontal displacements are given in Fig. 4. The five-segment fault model used to investigate slip distribution (dotted blue lines, also see Fig. 3), the Izmit earthquake epicenter and focal mechanism (35), and pre-earthquake seismicity (49) are also shown. Light lines are mapped or inferred faults (34). Izmit Bay is the E-W elongated bay on the east side of the Marmara Sea. The Hersek Delta is located on the



south shore of Izmit Bay about 10 km SE of station TUBI. MV, Mudurnu Valley fault. **Fig. 2. (right)** Map of observed postseismic GPS station displacements (black arrows) relative to ANKR (located at 39.89°N, 32.76°E) during the first 75 days following the earthquake. Error ellipses indicate 95% confidence intervals. Modeled station displacements (yellow arrows) were computed with the slip distributed dislocation model shown in Fig. 3C. Station names (four-character ID) indicate continuously operating sites installed within 48 hours following the main shock. Red dots indicate aftershocks of the first 30 days (33). The blue dotted line indicates the fault geometry used in the postseismic model inversions (note that the fault is extended to the east of the coseismic fault model to include the Düzce segment). The "beach ball" shows the location and focal mechanism of the  $M_w$  7.2, 12 November 1999, Düzce earthquake (35).

displacements, except for some sites along the easternmost Karadere segment (Fig. 2).

**InSAR data.** We have also examined the deformation field recorded by InSAR (interferometric synthetic aperture radar) (43). In this case, one 28-mm fringe in the interference pattern implies 75 mm of horizontal east-west displacement (44). The best coseismic interferograms (45) (Fig. 5, A and B) show more fringes and a higher fringe gradient than predicted from the slip distribution derived from GPS alone. The difference between the ERS-1 interferogram and the fringe pattern predicted from the GPS slip distribution (Fig. 6) shows at least 10 residual fringes, indicating that the east-west displacements inferred from ERS-1 are at least 70 cm larger than predicted by our GPS-derived coseismic fault model. Only a few tens of mm of this discrepancy can be attributed to postseismic deformation (Fig. 2). The large majority of the discrepancy reflects oversimplifications in the GPS-derived coseismic fault model and artifacts in the ERS-1 observations.

Near the Black Sea coast, the fringes in the interferograms follow the curves of the topographic relief, jogging sharply into two river valleys (Fig. 5B). Interpreted as coseismic strain, these fringe gradients are larger than expected in the far field 25 km north of the main fault trace. They are more likely a consequence of the radar signal's propagating through the heterogeneous troposphere. These artifacts can be as large as 3 cm in range over length scales as short as 10 km, as is apparent in the difference of the two best coseismic interferograms (Fig. 7). The bull's-eye pattern centered on Izmit indicates that the range increase is at least two fringes (6 cm) larger for the ERS-2 interferogram than for the ERS-1 interferogram.

The GPS measurements acquired at stations TUBI, KANT, and DUMT (Fig. 1) provide some support for the hypothesis of tropospheric perturbations. The bi-hourly estimates of tropospheric delay at zenith indicate between 4 and 10 cm of tropospheric thinning between the acquisition dates of the ERS-1 and ERS-2 images (46). These values are large enough to explain the artifacts in the fringe pattern. Yet their sign is opposite the tropospheric thickening suggested by the residual range increase in Fig. 6, perhaps because of short-scale variations between the interferogram and the three available GPS stations lying outside it.

The difference between the interferograms and our coseismic GPS estimates is 30 mm and 42 mm along the radar line of sight for the ERS-1 and ERS-2 interferograms, respectively. The discrepancies between the range changes estimated by InSAR and GPS do not show any obvious correlation with topographic elevation (47). They appear to be caused by tropospheric variations over distances shorter than the ~10-km spacing be-

tween GPS stations.

These results show that both the ERS-1 and ERS-2 interferograms are significantly contaminated by tropospheric artifacts. Accordingly, we have chosen not to include these InSAR results in our estimate of coseismic slip. The inversion procedure is particularly sensitive to gradients in the displacement field, which are, in turn, sensitive to errors in range along the steep radar line of sight. In the far field, at 50 km from the fault, an error of one 28-mm fringe in range can alter the estimate of slip on the fault by several meters. This may explain why models based on these InSAR observations tend to find more slip on the fault, and thus a higher total moment, than does our GPS-only solu-

tion. Using these interferograms to estimate the slip distribution and subtracting the postseismic GPS moment of  $2.91 \times 10^{19}$  Nm gives moments of  $3.35 \times 10^{20}$  Nm and  $3.88 \times 10^{20}$  Nm, for ERS-1 and ERS-2, respectively. This difference of 14% in moment is due mostly to the tropospheric variations over the single day that ERS-2 lags behind ERS-1. It also confirms that the ERS-2 interferogram contains a larger tropospheric contribution than does the ERS-1 result. In this case, it appears that tropospheric effects led to an overestimation of seismic moment. The slip distribution we estimated from the InSAR results yields a coseismic moment magnitude of about  $M_w = 7.7$ , which is substantially larger than the value of

**Fig. 3.** (A) Cross section (perspective view looking from south) of model fault, showing mapped surface offsets (open symbols) (30–32) compared to best-fitting GPS-derived surface slip model. (B) Coseismic distributed slip model (Izmit hypocenter is shown on the cross section). (C) Distributed postseismic strike slip along and below the Izmit earthquake rupture inverted from the GPS measurements of the first 75 days after the event. Note anti-correlation with coseismic slip, shown in (B). (D) Predicted slip distribution during first 2 postseismic months computed using a finite element model of a narrow viscously deforming shear zone below 10 km depth. The coseismic slip model in (B) was used to load the viscous shear zone (52). Note different color scale for slip in (B), (C), and (D).

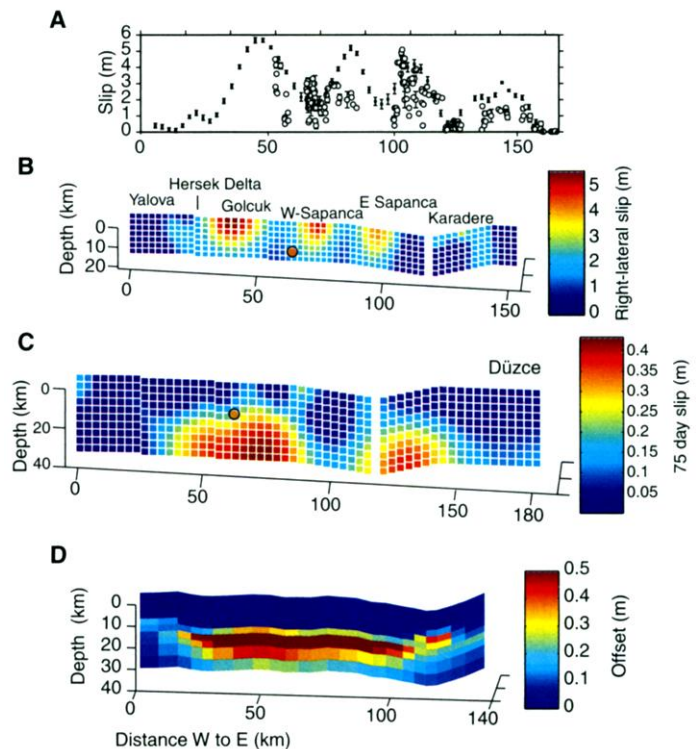
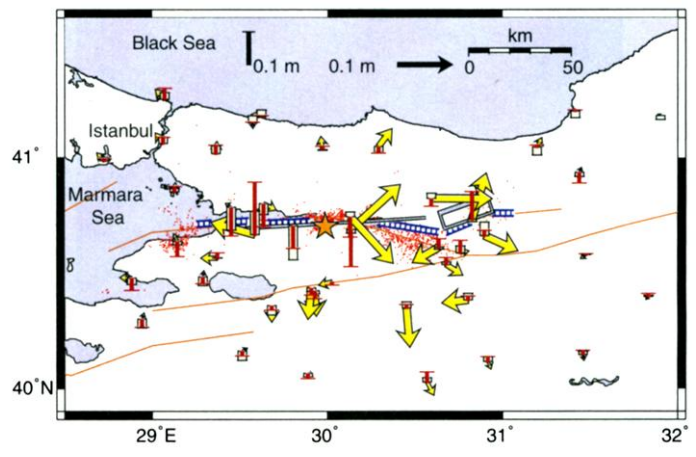


**Fig. 4.** Coseismic residual horizontal displacements not fit by five-segment model shown in cross section in Fig. 3B. Modeled and observed vertical displacements are shown by open and red bars, respectively. The surface projection of the two-segment (gray) and five-segment (dotted blue) fault models and the main shock epicenter (star) are also shown. Dots are aftershocks (17 August to 14 September 1999) (33).



$M_w = 7.5$  we estimated from the GPS measurements alone.

**Fault mechanics and the earthquake cycle.** The distribution of coseismic slip indicates that the Izmit earthquake nucleated on a relatively low-slip patch of the fault and propagated east and west, producing higher coseismic slip on adjacent fault patches (Fig. 3B). This slip distribution is supported by teleseismic waveform inversions that indicate an emergent  $P$  wave with long duration and a

fault rupture that propagated to the east, followed by an impulsive subevent west of the hypocenter (38, 48). We interpret the GPS-coseismic slip distribution to imply that the earthquake initiated on a patch of the fault that failed in part due to prior aseismic slip that impeded dynamic slip. This interpretation is supported by the occurrence of enhanced pre-earthquake microseismicity in the epicentral area (49, 50) (Fig. 1).

The hypothesis that the Izmit hypocentral

fault region may fail in part aseismically is further supported by the distribution of post-seismic afterslip. Rapid afterslip is concentrated on fault segments that experienced relatively little slip during the event and on segments below the coseismic rupture (Fig. 3). We interpret this to imply that these parts of the fault plane, including the hypocentral area, fail in part by creep. The shallow afterslip appears localized in velocity-strengthening (i.e., creeping) regions where dynamic

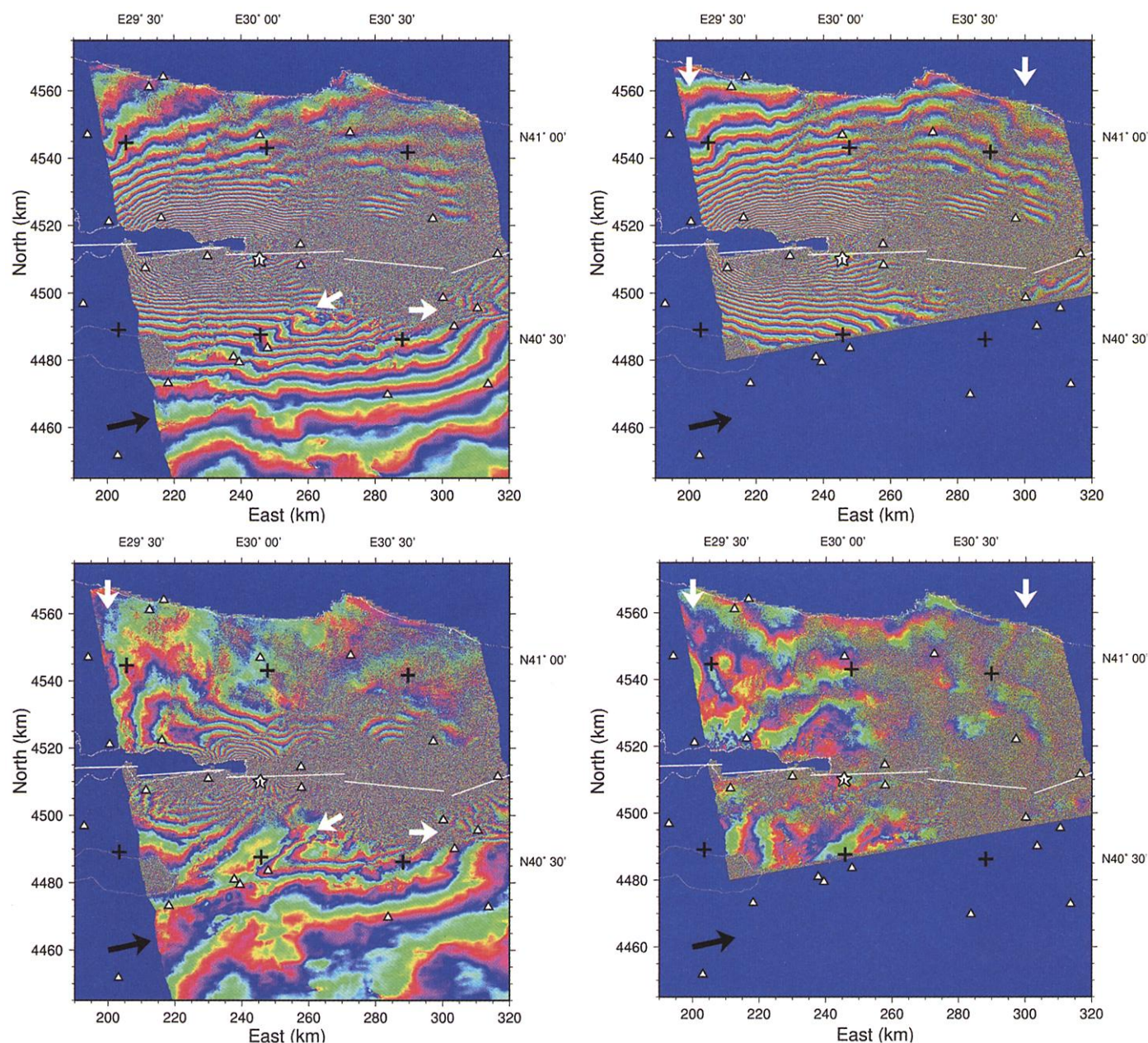


**Fig. 5. (A) (upper left)** Interferogram composed of two ERS-1 images acquired on 12 August 1999 and 16 September 1999. White arrows show minor displacements on secondary faults. **(B) (upper right)** Interferogram composed of two ERS-2 images acquired on 13 August 1999 and 17 September 1999. White arrows show anomalous jogs where the fringes follow the topographic relief indicating tropospheric artifacts. One fringe represents 28 mm of change in radar range along the radar line of sight. The surface projection of the radar line of sight (black arrow), CMT

epicenter (white star), GPS stations (triangles), coastlines (thin white lines), traces of modeled fault (thick white segments), and registration marks at multiples of  $1/2$  degree in latitude and longitude (black crosses) are also shown (45). **Fig. 6. (lower left)** Residual interferogram calculated by subtracting the fringe pattern simulated using the GPS-derived coseismic slip distribution (Fig. 3B) from the interferogram observed by ERS-1. **Fig. 7. (lower right)** Difference between ERS-1 and ERS-2 interferograms.

slip was impeded (5). Postseismic slip apparently extended to near the base of the crust, at 30 to 36 km deep (51). A finite element model simulation of the response of a narrow, vertical viscoelastic fault zone below the coseismic rupture produces a comparable offset pattern (Fig. 3D) (52).

We hypothesize that the distribution of coseismic and postseismic slip on the Izmit rupture reflects (i) geometric segmentation of the Izmit rupture represented by step-overs and bends and (ii) variations in the mechanical properties of the fault zone consisting of velocity-weakening patches of high seismic moment release and velocity-strengthening patches that fail in part by creep and experience reduced dynamic slip. The abrupt drop in coseismic slip on the west end of the rupture and the absence of significant afterslip on the Yalova segment (in contrast to large afterslip below and to the east of the high slip patch) are likely due to an extensional, right step in the fault near the Hersek Delta (34). In contrast to this behavior at the west end of the Izmit coseismic rupture, afterslip apparently extended east of the eastern end of the rupture (Karadere segment), which possibly helped to trigger the 12 November 1999,  $M_w = 7.2$ , Düzce earthquake that extended the Izmit rupture about 40 km further east (30, 53) (Fig. 2). The history of multiple and sequential earthquakes on the North Anatolian fault (54) suggests that triggered events are typical of the fault as a whole. If this mechanical behavior is also characteristic of the earthquake generation and nucleation process on fault segments to the west of the Izmit rupture, we would expect that evidence of deep aseismic slip might indicate future earthquake nucleation points and that creep transients could precede future ruptures.

As the zone of postseismic afterslip overlaps with the inferred locking depth in the years before the earthquake, our observations support an earthquake cycle model in which (i) steady interseismic deformation occurs in the upper mantle and lower crust accommodated by localized shear and distributed ductile flow; (ii) aseismic faulting, which is highly accelerated following the sudden stress pulse from a large earthquake, occurs at mid- to lower crustal levels; and (iii) brittle seismic rupture occurs in the upper crust, followed by afterslip along some portions of the fault. Continued observations of postseismic deformation in the next several years will further elucidate the possible contribution of accelerated viscous flow in the lower crust to the active deformation and loading of neighboring faults (55).

#### References and Notes

- Y. Okada, *Bull. Seismol. Soc. Am.* **75**, 1135 (1985).
- T. Arnadottir and P. Segall, *J. Geophys. Res.* **99**, 21835 (1994).
- J. Freymuller, N. E. King, P. Segall, *Bull. Seismol. Soc. Am.* **84**, 646 (1994).
- S. T. Tse and J. R. Rice, *J. Geophys. Res.* **91**, 9452 (1986).
- C. H. Scholz, *Geol. Rdsch.* **77**, 319 (1988).
- F. F. Pollitz, G. Peltzer, R. Bürgmann, *J. Geophys. Res.* **105**, 8035 (2000).
- G. C. P. King, R. S. Stein, J. Lin, *Bull. Seismol. Soc. Am.* **84**, 935 (1994).
- R. S. Stein, A. A. Barka, J. H. Dieterich, *Geophys. J. Int.* **128**, 594 (1997).
- R. A. Harris, *J. Geophys. Res.* **103**, 24347 (1998).
- A. Hubert-Ferrari *et al.*, *Nature* **404**, 269 (2000).
- A. Nur and G. Mavko, *Science* **183**, 204 (1974).
- F. F. Pollitz, *Bull. Seismol. Soc. Am.* **82**, 422 (1992).
- P. Molnar *et al.*, *Science* **286**, 516 (1999).
- S. J. Bourne, P. C. England, B. Parsons, *Nature* **391**, 655 (1998).
- R. H. Sibson, *Annu. Rev. Earth Planet. Sci.* **14**, 149 (1986).
- L. E. Gilbert, C. H. Scholz, J. Beavan, *J. Geophys. Res.* **99**, 23975 (1994).
- J. Deng, M. Gurnis, H. Kanamori, E. Hauksson, *Science* **282**, 1689 (1998).
- W. Thatcher, *J. Geophys. Res.* **88**, 5893 (1983).
- J. C. Savage, *J. Geophys. Res.* **95**, 4873 (1990).
- W. Thatcher, *J. Geophys. Res.* **100**, 3885 (1995).
- Web figs. 1 through 4 and Web tables 1 and 2 are available at Science Online at [www.sciencemag.org/feature/data/1050250.shl](http://www.sciencemag.org/feature/data/1050250.shl).
- M. N. Toksoz, A. F. Shakal, A. J. Michael, *Pageoph* **117**, 1258 (1979).
- S. S. Nalbant, A. Hubert, G. C. P. King, *J. Geophys. Res.* **103**, 24469 (1998).
- C. Straub, H.-G. Kahle, C. Schindler, *J. Geophys. Res.* **102**, 27587 (1997).
- M. E. Ayhan *et al.*, paper presented at the 1999 International Union of Geodesy and Geophysics Annual Meeting, Birmingham, UK, 18 to 30 July 1999.
- N. Yalcin *et al.*, paper presented at the 1999 International Union of Geodesy and Geophysics Annual Meeting, Birmingham, UK, 18 to 30 July, 1999.
- S. McClusky *et al.*, *J. Geophys. Res.* **105**, 5695 (2000).
- At sites for which a well-constrained preseismic velocity estimate exists, the expected displacement and associated uncertainty were extrapolated from the last pre-earthquake measurement to the time of the earthquake. We invert the observed preseismic velocity field (27) for slip on a dislocation buried from 20 to 3000 km below the Izmit earthquake rupture zone and extending sufficiently to the east and west to eliminate fault end effects. This simple model with a deep slip rate of  $27 \pm 1$  mm/year below the Izmit region fits the GPS velocities within their uncertainties with a standard deviation of 2.2 mm/year. The model velocities were used to establish pre-earthquake coordinates for sites without measured preseismic velocities. The largest magnitude of the uncertainty for this correction is 13 mm (95%) for a site whose last pre-earthquake occupation was in September 1996.
- We used the afterslip model to project station positions measured after the earthquake to the time immediately following the main shock. The standard deviation to the measured postearthquake velocities is 45 mm/year. The largest magnitude of the uncertainty for this correction is 9 mm (95%) for a station observed 40 days after the earthquake.
- A. Barka *et al.*, *EOS* **80**, F647 (1999).
- E. Herece, *Kocaeli Depremi kirik Haritasi ve Ilgili Gozlem Noktalarinin Tanimlari* (MTA, Ankara, Turkey, 1999).
- R. Bilham, unpublished data.
- M. Ergin *et al.*, *EOS* **80**, F663 (1999).
- A. Barka, *Active Tectonics of Northwestern Anatolia: The Marmara Poly-Project* (ETH, Zurich, 1997), pp. 55–87.
- Focal Mechanism from Harvard CMT Catalog ([www.seismology.harvard.edu/CMTsearch.html](http://www.seismology.harvard.edu/CMTsearch.html)).
- Using nonlinear inversion techniques to solve for the best-fitting geometry and slip vector on two rectangular dislocations [e.g., R. Bürgmann, P. Segall, M. Lisowski, J. Svarc, *J. Geophys. Res.* **102**, 4933 (1997)] results in a model with a western, 87°-striking, 97-km long, 16-km-wide segment that dipped 90° and slipped 2.8 m right-lateral and 0.28 m south-side up.
- The second dislocation is located along the Karadere segment, 25 km by 19 km, that dipped 63° to the north, and slipped 1.6 m right-lateral and 0.5 m south-side up. The distribution of aftershocks to the north of the Karadere segment and the geometry of the subsequent 12 November 1999 Düzce event support a dipping eastern Izmit rupture. The misfit, or weighted residual sum of squares of this model was 6929 [ $WRSS = (d_{obs} - d_{mod})^T \times cov^{-1} \times (d_{obs} - d_{mod})$ ], where  $d_{obs}$  and  $d_{mod}$  are the observed and modeled motions, respectively, T is transpose, and cov is the data covariance matrix).
- We applied smoothing using a finite difference approximation of the Laplacian and non-negativity (right-lateral slip only) constraints to avoid models with unreasonable slip patterns that may be favored by a free inversion. We evaluated synthetic slip models of varying complexity to determine the amount of smoothing used in the final inversion results.
- M. N. Toksoz, C. G. Doll, V. F. Cormier, *EOS* **80**, F647 (1999). For the geodetic moment calculation, we assumed a rigidity of 30 GPa.
- F. Tajima, D. Dreger, L. Breger, R. Uhrhammer, B. Romanowicz, *EOS* **80**, F669 (1999).
- T. Parsons, S. Toda, R. S. Stein, A. Barka, J. H. Dieterich, *Science* **288**, 661 (2000).
- E. R. Ivins, *J. Geophys. Res.* **105**, 3229 (2000).
- The total moment  $M_0$  of 4397 aftershocks from 17 August to 14 September 1999 was  $2.5 \times 10^{18}$  Nm using  $\log M_0 = 1.2 m_l + 17.5$  [D. E. Chavez and K. F. Priestley, *Bull. Seismol. Soc. Am.* **75**, 583 (1985)], where  $m_l$  is the local magnitude.
- D. Massonnet and K. L. Feigl, *Rev. Geophys.* **36**, 441 (1998).
- The unit vector pointing from the ground to the satellite along the radar line of sight has east, north, and upward components of  $-0.087$ ,  $0.371$ , and  $+0.925$ , respectively, at the epicenter.
- The amplitudes of ambiguity for ERS-1 and ERS-2 are 337 and 520 m, respectively. All four images were acquired at 20:14 UTC (Universal Time Coordinated). The orbit numbers are 42229 and 42730 for ERS-1, and 22556 and 23057 for ERS-2. The postearthquake orbital trajectories were optimized for this application by the European Space Agency at the behest of F. Sarti. We use the DIAPASON software developed by the French Space Agency, CNES, and licensed to GDR InSAR. The interferograms have been filtered using the ps\_filt2 program provided by Z. Lu to implement the algorithm of R. M. Goldstein and C. L. Werner [*Geophys. Res. Lett.* **25**, 4035 (1998)].
- For the ERS-1 acquisition dates, the changes in tropospheric zenith delay estimated from GPS are  $-94$  mm at TUBI,  $-94$  mm at KANT, and  $-73$  mm at DUMT. For the ERS-2 dates, they are  $-84$  mm,  $-104$  mm, and  $-41$  mm, respectively. The change in ERS radar slant range would be larger by a factor of  $1/\sin(23^\circ)$ , or 9%.
- See Web fig. 4 (21), showing the difference in range change, along the radar line of sight, between the ERS-1 and GPS determinations. The eastward slope of  $-0.2$  mm/km may be due to orbital errors. Tropospheric artifacts have been observed to correlate with topographic elevation on Mount Etna [F. Beauducel, P. Briole, J. L. Froger, *J. Geophys. Res.*, in press].
- A. Pinar *et al.*, *EOS* **80**, F648 (1999).
- The Council of the National Seismic System Worldwide Earthquake Catalog is archived at the Northern California Earthquake Data Center for the period 1990 to 16 August 1999 and is available at <http://quake.geo.berkeley.edu/cnss>.
- Increased levels of microseismicity along the San Andreas fault system are correlated with segments that are found to experience high levels of interseismic creep, such as the central creeping segment between San Juan Bautista and Parkfield, and the Hayward and Calaveras faults [e.g., W. L. Ellsworth, in *The San Andreas Fault System, California*, R. E. Wallace, Ed. (U.S. Geological Survey, Washington, DC, 1990), vol. 1515, pp. 153–187].
- J. Makris and C. Stobbe, *Marine Geol.* **55**, 347 (1984).
- A simple model of a viscoelastic vertical shear zone from 10 to 40 km depth with a viscosity/shear-zone-width ratio of  $2 \times 10^{13}$  Pa s  $m^{-1}$  (e.g., a 1-km-wide shear zone

with viscosity of  $2 \times 10^{16}$ ) produces an acceptable fit to the data (not shown) and general similarity with the inverted slip distribution (Fig. 3, C and D).

53. E. H. Hearn, R. Burgmann, R. Reillinger, *EOS* **81**, S307 (2000).  
54. N. N. Ambraseys *Tectonophysics* **9**, 143 (1970).

55. We thank B. King, T. Herring, E. Price, P. Segall, T. Wright, and D. Massonnet for helpful discussions. Raw ERS synthetic aperture radar (SAR) and orbital data were provided by the European Space Agency. We used the digital elevation model calculated by E. Fielding from ERS Tandem data in advance of

publication. Supported in part by a grant from the World Bank to TUBITAK MRC and by MIT grants NASA NAG5-6145, NSF EAR-9909730, and NSF INT-9909619.

9 March 2000; accepted 22 June 2000

## Regulation of Absorption and ABC1-Mediated Efflux of Cholesterol by RXR Heterodimers

J. J. Repa,<sup>1</sup> S. D. Turley,<sup>2</sup> J.-M. A. Lobaccaro,<sup>1\*</sup> J. Medina,<sup>3</sup> L. Li,<sup>3</sup> K. Lustig,<sup>3</sup> B. Shan,<sup>3</sup> R. A. Heyman,<sup>4†</sup> J. M. Dietschy,<sup>2</sup> D. J. Mangelsdorf<sup>1‡</sup>

Several nuclear hormone receptors involved in lipid metabolism form obligate heterodimers with retinoid X receptors (RXRs) and are activated by RXR agonists such as retinoids. Animals treated with retinoids exhibited marked changes in cholesterol balance, including inhibition of cholesterol absorption and repressed bile acid synthesis. Studies with receptor-selective agonists revealed that oxysterol receptors (LXRs) and the bile acid receptor (FXR) are the RXR heterodimeric partners that mediate these effects by regulating expression of the reverse cholesterol transporter, ABC1, and the rate-limiting enzyme of bile acid synthesis, CYP7A1, respectively. Thus, these RXR heterodimers serve as key regulators of cholesterol homeostasis by governing reverse cholesterol transport from peripheral tissues, bile acid synthesis in liver, and cholesterol absorption in intestine.

Several orphan nuclear hormone receptors regulate cholesterol homeostasis. The liver X receptors (LXR $\alpha$ /NR1H3 and LXR $\beta$ /NR1H2) and farnesoid X receptor (FXR/NR1H4) (1) are bound and activated by oxysterols and bile acids, respectively, and regulate the expression of genes involved in cholesterol metabolism [reviewed in (2–4)]. The LXRs mediate oxysterol-regulated transcriptional induction of cholesterol  $7\alpha$ -hydroxylase (CYP7A1), the rate-limiting enzyme of the classic bile acid biosynthetic pathway. Lxr $\alpha$ -knockout mice fed a high cholesterol diet fail to up-regulate CYP7A1 expression and bile acid production, thereby accumulating cholesterol ester in their livers (5). This phenotype is exacerbated in Lxr $\alpha$ / $\beta$  double-knockout mouse strains (6). Additional LXR

target genes involved in lipid metabolism include the human cholesterol ester transfer protein (CETP), which translocates cholesterol ester between lipoprotein fractions (7), and the murine adenosine triphosphate-binding cassette transporter 8 (ABC8), which has been implicated in macrophage lipid flux (8). FXR mediates bile acid-dependent repression of the CYP7A1 gene (9, 10) by inducing the transcription of small heterodimer partner (SHP) (11), an orphan receptor that is a transcriptional repressor of CYP7A1 expression (12). In a similar manner, FXR also regulates expression of several proteins involved in bile acid metabolism, including sterol  $12\alpha$ -hydroxylase (CYP8B1), which controls the relative production of the primary bile acids, the intestinal bile acid binding protein, and the phospholipid transfer protein (9, 13, 14).

LXRs and FXR form obligate heterodimers with retinoid X receptors (RXRs) and belong to a subclass of nuclear hormone receptors that are activated by RXR agonists. We exploited this characteristic in animal studies by administering retinoid LG268, a highly specific RXR ligand (15), to identify nuclear receptor-mediated changes in cholesterol balance and the receptor-regulated genes responsible for those changes. This approach had several advantages: It allowed a more global analysis of nuclear receptor-mediated events by allowing simulta-

neous assessment of several permissive receptors including LXRs, FXR, and the peroxisome proliferator-activated receptors (PPARs); it avoided complications that would arise from the use of oxysterols to activate LXR, because these compounds also affect the SREBP signaling pathway (16); and the effective doses and pharmacokinetics of LG268 had been established previously (17). Here, we show that retinoids affect cholesterol absorption, transport, and catabolism in rodents through at least two pathways that regulate the transcription of key target genes. In one pathway, activation of the RXR/FXR heterodimer repressed CYP7A1 expression, resulting in decreased bile acid synthesis and cholesterol absorption. In the second pathway, activation of the RXR/LXR heterodimer by either a retinoid or LXR agonist effectively blocked cholesterol absorption and induced reverse cholesterol transport in peripheral tissues. This effect was coincident with the increased expression in intestine and macrophages of ABC1, a gene product responsible for efflux of cellular free cholesterol (18–20).

**Retinoid effects on cholesterol homeostasis.** Administration of the retinoid LG268 to mice resulted in dose-dependent inhibition of cholesterol absorption (Fig. 1A). A fecal dual-isotope method was used to monitor cholesterol absorption (21), which measures the ratio of fecal excretion of [ $^3$ H]sitostanol (which is not absorbed) to [ $^{14}$ C]cholesterol (which is variably absorbed). LG268 at a dose of 1.4 mpk (equivalent to 0.0007% of the diet) resulted in a 50% reduction in cholesterol absorption, and a dose of 14 mpk resulted in complete inhibition. In addition, retinoid treatment prevented the appearance of [ $^{14}$ C]cholesterol in the serum, confirming that no dietary cholesterol was transported across the enterocyte into the circulation (22). LG268 also inhibited cholesterol absorption in the Golden Syrian hamster, with a reduction of 37% at 3 mpk LG268 and 76% at 30 mpk LG268. Thus, the effect of retinoid on cholesterol absorption was not species specific.

At all doses tested, decreased absorption elicited by retinoid prevented accumulation of liver cholesterol, even when mice were fed a high (0.2%) cholesterol diet (Fig. 1B). In addition, total serum cholesterol levels were not elevated by retinoid administration, but the relative level of high-density lipoprotein (HDL) cholesterol increased (Fig. 1C). The effect of LG268 was specific for cholesterol and had no consequence on general lipid absorption, mostly triacylglycerol (Fig. 1D). Decrease in lipid absorption observed at higher doses of retinoid can be accounted for by the contribution of

<sup>1</sup>Howard Hughes Medical Institute and Department of Pharmacology, <sup>2</sup>Department of Internal Medicine, University of Texas Southwestern Medical Center, 5323 Harry Hines Boulevard, Dallas, TX 75390–9050, USA. <sup>3</sup>Tularik, Two Corporate Drive, South San Francisco, CA 94080, USA. <sup>4</sup>Ligand Pharmaceuticals, 10255 Science Center Drive, San Diego, CA 92121, USA.

\*Present address: Physiologie Comparée-Endocrinologie Moléculaire, UMR CNRS 6547-GEEM, Université Blaise Pascal, 63177 Aubière Cedex, France.

†Present address: X-Ceptor Therapeutics, 4757 Nexus Centre Drive, San Diego, CA 92121, USA.

‡To whom correspondence should be addressed. E-mail: davo.mango@utsouthwestern.edu